Check for updates

Structural correlation of a nanoparticle-embedded mesoporous CoTiO₃ perovskite for an efficient electrochemical supercapacitor

Narasimharao Kitchamsetti,[a] Ram J. Choudhary, [iD][b] Deodatta M. Phase [iD][b] and Rupesh S. Devan [iD] *[a]

We synthesized mesoporous cobalt titanate (CTO) microrods *via* the sol–gel method as an outstanding working electrode for the supercapacitor. The mesoporous CTO microrods were amassed in hexagonal shapes of an average width of ∼670 nm, and were composed of nanoparticles of average diameter ∼41 nm. The well crystalline CTO microrods of the hexagonal phase to the $R\bar{3}$ space group possessed an average pore size distribution of 3.92 nm throughout the microrod. The mesoporous CTO microrods with increased textural boundaries played a vital role in the diffusion of ions, and they provided a specific capacitance of 608.4 F g⁻¹ and a specific power of 4835.7 W kg⁻¹ and a specific energy of 9.77 W h kg⁻¹ in an aqueous 2 M KOH electrolyte, which was remarkably better than those of Ti, La, Cr, Fe, Ni, and Sr-based perovskites or their mixed heterostructures supplemented by metal oxides as an impurity. Furthermore, the diffusion-controlled access to the OH⁻ ions (0.27 μs) deep inside the microrod conveyed high stability, a long life cycle for up to 1950 continuous charging–discharging cycles, and excellent capacitance retention of 82.3%. Overall, the mesoporous CTO shows its potential as an electrode for a long-cycle supercapacitor, and provides opportunities for additional enhancement after developing the core–shell hetero-architecture with other metal oxide materials such as MnO_2, and TiO_2.

1 Introduction

The fast growth of the global population and massive industrialization of human civilization have induced enormous pressure on the environment, and have also brought forward a severe concern about the energy crisis. The continuous improvement in energy generation and storage is of great importance to meet worldwide energy challenges for a sustainable supply of low-cost and clean energy. The amalgamation of abundant renewable energies (*i.e.*, biofuels and solar energy) and versatile electrochemical energy conversion and storage devices like supercapacitors,[1] fuel cells,[2] and batteries[3] may offer an ideal energy system for the future. Still, it is not yet efficiently functionalized to serve the needs of society. Batteries known for their specific energy fail to provide improved specific power and compete with a supercapacitor. The balancing of the specific energy and specific power of supercapacitors is of vital importance to support the daily energy needs, and also to overcome the sudden power loss. The automotive and power electronics industry continues to hint that supercapacitors have the potential to replace batteries in the coming future upon reducing the short circuits and self-discharge, and maintaining

the long cycle lifetime. Therefore, hierarchical and mesoporous hybrid nanostructures are attracting considerable attention owing to the largest accessible surface area, along with good interconnections for energy storage. The pore size and specific surface area accessible for ion diffusion significantly influence the energy storage mechanism.

Due to their high surface area and short ion diffusion length, nanostructured transition metal oxides have shown tremendous electrochemical performance that is superior to that of bulk. Among the well-studied various metal oxides such as TiO_2, MnO_2, Fe_2O_3, NiO, Ta_2O_5, MoO_2, V_2O_5, Nb_2O_5, and Co_3O_4,[4] the oxides of Co and Ti exhibited decent and long cycling electrochemical performances.[5–8] Among these various pseudocapacitive materials, TiO_2 is widely used in energy storage and conversion, *i.e.*, supercapacitors, Li-ion batteries, solar cells, photocatalysis, and sensors. This is due to its chemical and thermal stability, high aspect ratio structure, excellent ionic or electronic charge transfer, wide bandgap, and environmental friendliness. Moreover, TiO_2 resembles the conventional electric double-layer capacitor, which contributes to the non-faradaic mechanism with very low specific capacitance (C_s).[9] Although pristine TiO_2 reveals a low electrochemical performance, it shows excellent stability for the continuous charging–discharging of 10000 cycles[5] than any other metal oxide in its pristine form. Similarly, Co_3O_4 has been explored as an electrode material for supercapacitors due to its tunable

[a]Discipline of Metallurgy Engineering and Materials Science, Indian Institute of Technology Indore, Simrol, Indore 453552, India. E-mail: rupesh@iiti.ac.in

[b]UGC-DAE Consortium for Scientific Research, Khandwa Road, Indore 452001, India

morphology, chemical, and thermal stability, redox activity, and high theoretical C_s.[8] However, very limited effort has been made to utilize the hetero-architectures of TiO_2 and Co_3O_4 as electrode materials for supercapacitors.[9-11] Perovskites, with the generalized formula of ABO_3 (where A and B are Ti and Co, respectively), have involved great interest owing to their excellent optical,[12,13] electronic,[14] catalytic,[15] ferroelectric,[12] and magnetic properties.[16] Recently, Imani *et al.*[17] reported microwave-irradiated $NiTiO_3$ nanoparticles as an electrode for supercapacitor applications. The results indicated an acceptable C_s of 257 F g^{-1} at a scan rate of 10 mV s^{-1} with a good reversible redox reaction, and a capacitance retention of ~92% after 1000 cycles. In addition to this, Pejman *et al.*[18] synthesized $NiMnO_3$/C nanocomposite electrodes for supercapacitors that exhibit a C_s value of 285 F g^{-1} at a current density of 1 A g^{-1}, and excellent cycling stability with 93.5% capacitance retention over 1000 cycles. Recently, Huang *et al.* derived CTO mesoporous micro-prisms from the bimetal–organic framework as an anode material for sodium-ion batteries, and observed 90.1% (@ 5 A g^{-1}) capacity retention for 2000 cycles in Na$^+$ ions.[19] However, to the best of our knowledge, no reports are available in the literature on the utilization of $CoTiO_3$ as an electrode for a supercapacitor. Therefore, we report here the utilization of the $CoTiO_3$ compound as the electrode for a supercapacitor. Highly porous CTO microrods were synthesized *via* the sol–gel route. The effect of functional groups on the synthesis of the mesoporous CTO microrods was examined by FTIR. The structural properties were analyzed by Raman spectroscopy and X-ray diffraction. The surface morphologies and chemical composition of the CTO microrods were examined using field emission scanning electron microscopy (FESEM), and X-ray photoemission spectroscopy (XPS), respectively. The molar ratio-dependent diffusion of OH$^-$ ions from the aq. KOH electrolyte along the surface of the mesoporous CTO rods was examined from the drop shape analyzer. The effect of the mesoporous morphology of the CTO rods consisting of interconnected nanoparticles on the electrochemical properties of CTO was investigated systematically utilizing cyclic voltammetry (CV), galvanostatic charge–discharge (GCD) and impedance spectroscopy (EIS) in KOH electrolyte. The mesoporous CTO rods delivered a Cs value of 608.4 F g^{-1}, a specific power of 4835.7 W kg^{-1}, a specific energy of 9.77 W h kg^{-1}, and long cyclic stability.

2 Experimental

Mesoporous CTO microrods were synthesized *via* a simple sol–gel method utilizing cobalt(II) acetate tetrahydrate (Co(CH$_3$-COO)$_2$; 99.999%), tetrabutyl titanate polymer (Ti(OBu)$_4$), ethylene glycol (AR grade), and ethanol (ACS reagent, 96%). Stoichiometric amounts of Co(CH$_3$COO)$_2$ and Ti(OBu)$_4$ in a 1 : 1 molar proportion were dissolved in the ethylene glycol (EG) at room temperature under constant stirring to synthesize the $CoTiO_3$ precursor. The red-colored solution gradually turned into a light pink solution of metal–glycolate polymer chain-like structure, and was further stirred for the next 1 h to obtain the Co–Ti–EG powder. The Co–Ti–EG powder was washed with

ethanol and deionized water several times, and further annealed at 600 °C under ambient conditions for 5 h to ensure the formation of the crystalline $CoTiO_3$ green powder. The crystalline and structural properties of the annealed CTO powder were characterized using XRD (D2-phaser Bruker) equipped with Cu Kα radiation ($\lambda = 1.54$ Å), and Raman spectroscopy (Renishaw inVia reflex spectrometer, 532 nm laser), respectively. The effect of functional groups on the features of the CTO rods was examined from FTIR spectroscopy (PerkinElmer Spectrum, one FTIR spectrometer). The surface morphological features were identified utilizing field-emission scanning electron microscopy (FESEM, JEOL JSM-6500F). The elemental analysis was carried out using energy dispersive spectroscopy (Oxford EDS X-MAX 20 mm). The chemical states and electronic structure of the mesoporous CTO rods were identified using an X-ray photoelectron spectrometer (XPS, Thermo Scientific Inc. K-alpha) with a microfocus mono-chromated Al Kα X-ray source. The surface area and pore size distribution of the powder were calculated from nitrogen adsorption and desorption isotherms based on the Brunauer–Emmett–Teller and Barrett–Joyner–Halenda methods, respectively. The surface wettability was evaluated for different concentrations of the KOH electrolyte using a drop shape analyzer (DSA-25, Kruss GmbH, Hamburg, Germany). The electrochemical performance of the mesoporous $CoTiO_3$ microrod was examined using an electrochemical workstation (Autolab PGSTAT302N). The supercapacitor consisted of a CTO-coated Ni foam as the working electrode, a platinum foil as the counter electrode, a saturated calomel electrode as the reference electrode, and aqueous KOH as an electrolyte. It was examined at room temperature to investigate the potentials of the mesoporous CTO rods in the electrochemical performance.

3 Results and discussion

The FTIR spectra in Fig. 1 indicate the effect of metal–organic Co–Ti–EG glycolate on the synthesis of mesoporous CTO rods. There were a greater number of peaks observed for the as-synthesized Co–Ti–EG glycolate powder (Fig. 1(b)), which disappeared after annealing at a temperature of 600 °C (Fig. 1(a)). The peaks centered at 3328, 1452, 1050, and 876 cm^{-1} were assigned to the υ_{OH}, δ_{OH}, υ_{CO}, and γ_{OH} bands of the C–O and O–H bonds in the –CH$_2$–OH moiety, respectively.[19] In addition, the peaks centered at 2472, 1818, 1314, and 1210 cm^{-1} were assigned to the υ_{OH}, $\upsilon_{C=O}$, δ_{OH}, and υ_{CO} bands of the C=O, C–O, and O–H bonds in the –COOH group, respectively.[19] The peaks centered at 2828 and 2923 cm^{-1} were indexed to the symmetric and anti-symmetric stretching vibrations, respectively, of the C–H bonds in the –CH$_2$– group, instead of the –CH$_3$ group.[20] However, all of these peaks assigned to the various organic components might have decomposed into CO, CO_2, and H_2O, and disappeared after annealing the as-synthesized CTO powder at a temperature of 600 °C. Therefore, the presence of weak bands only between 400 to 800 cm^{-1} was assigned to the stretching vibrations of the metal ions of the mesoporous CTO rods (Fig. 1(a)).[20]
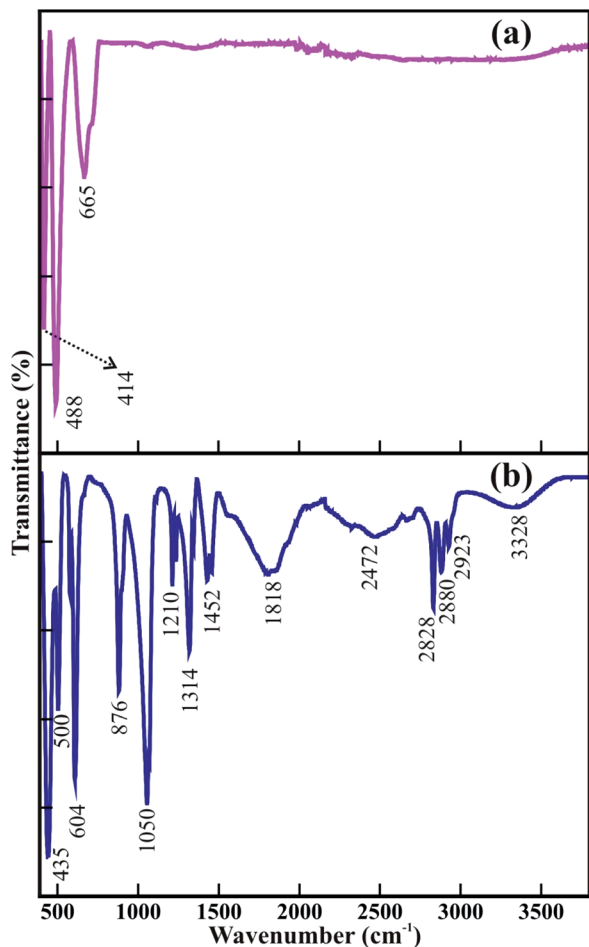
Fig. 1 FTIR spectra of (a) CTO microrod obtained after annealing (b) as-prepared Co–Ti–EG polymer chain precursor.
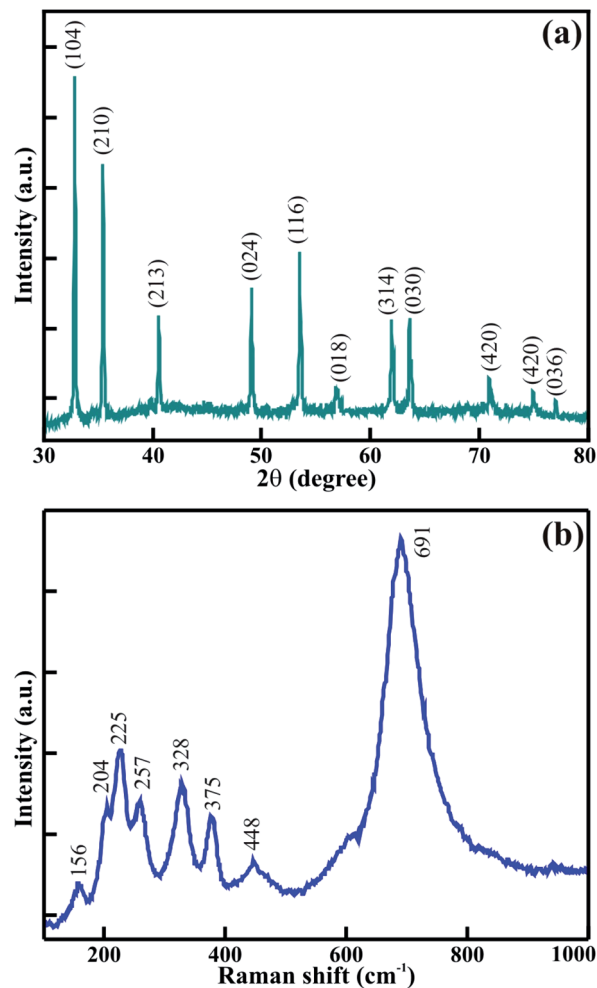

Fig. 2 (a) XRD pattern and (b) Raman spectrum of mesoporous CTO microrods.

Fig. 2(a) shows the X-ray diffraction pattern of the annealed CTO microrod. The hexagonal crystal structure of the space group $R\bar{3}$ (with the lattice parameters $a = b = 5.0654$, $c = 13.9209$ Å; $\alpha = \beta = 90°$ and $\gamma = 120°$ (JCPDS: 72-1069)) was assigned to the mesoporous CTO microrods. The diffraction peaks identified at $2\theta = 32.8, 35.4, 40.5, 49.08, 53.5, 56.9, 61.9, 63.6, 70.9, 74.9,$ and $77.1°$ were indexed as the (104), (210), (213), (024), (116), (018), (314), (030), (1010), (420), and (036) lattice planes, respectively. The well indexing of all diffraction peaks confirmed the formation of pure crystalline mesoporous CTO microrods without impurity phases, such as TiO_2 and Co_3O_4. Furthermore, the Raman spectroscopic analysis shown in Fig. 2(b) was executed to understand the structural properties of the CTO rods. A total of 8 significant Raman bands observed at 691, 448, 375, 328, 257, 225, 204, and 156 cm^{-1} were consistent with the earlier reported values for CTO nanoparticles and micro-prisms.[19,21] The strongest Raman mode observed at 691 cm^{-1} was assigned to the high frequency vibrational mode of the CoO_6 octahedra known as the symmetry stretching mode, and the other remaining Raman modes were assigned to the lattice vibrations of the phonon modes.[19,21] The observed Raman spectrum confirmed the absence of the other additional

bands corresponding to Co_3O_4, TiO_2, and the D/G bonds of carbon. Thus, the consistency of the Raman spectra with the XRD analysis also confirmed the formation of the pristine CTO rods.

The surface morphology was examined using FESEM to understand the effect of EG on the growth of the mesoporous CTO microrods. Fig. 3(a) shows the surface morphology of the as-synthesized CTO rods. The hexagonal shaped rods with a smooth surface and clearly visible textural boundaries were composed of Co–Ti–EG glycolate chains, and grown to the average diameter of ~1.1 μm. These rods of Co–Ti–EG chains were further subjected to annealing at 600 °C. The smooth surface converted into the particle-like appearance without altering the hexagonal morphology of the rods (Fig. 3(b)). Co–Ti–EG glycolate was converted into intact CTO nanoparticles after the selective removal of EG glycolate on annealing. The well crystalline CTO nanoparticles were interconnected with adjacent nanoparticles, while maintaining the hexagonal morphological feature of the as-synthesized samples (Fig. 3(c)). The CTO nanoparticles of the average diameter of 40.7 (± 0.5) nm resulted in mesoporous rods of the average diameter
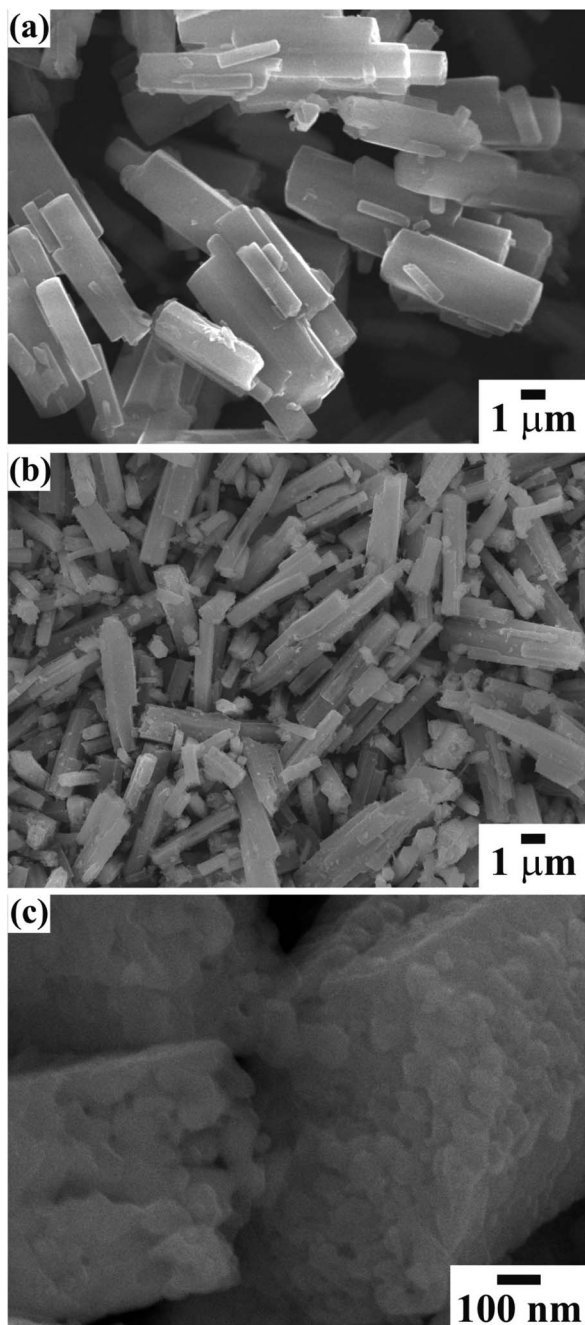
Fig. 3 FESEM image of (a) as-synthesized and (b) annealed CoTiO₃ microrod. (c) The high-magnification FESEM image confirms the formation of mesoporous CoTiO₃ microrod composed of hierarchically interlinked nanoparticles.
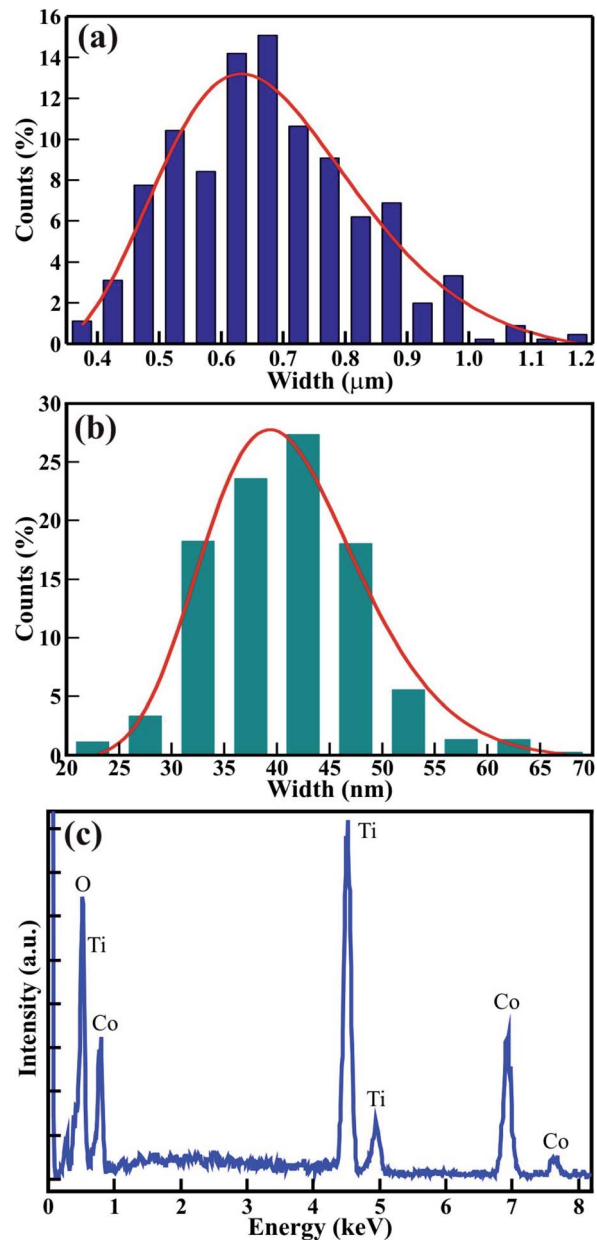

Fig. 4 (a and b) Statistical histogram of the width distribution microrods and nanoparticles, respectively, and (c) EDS spectra of mesoporous CTO microrods.

of 0.67 (±0.2) μm. Moreover, the formation of CTO nanoparticles that culminated in the mesoporous rods might be the result of the evaporation of the glycolate precursors.

A statistical histogram of the width distribution of the hexagonal rods and nanoparticle diameter is shown in Fig. 3(a) and (b), respectively. It shows that all of the nanoparticles and rods were smaller than 70 nm and 1.2 μm, but most of them fell in the range of 30 to 50 nm and 0.6 to 0.75 μm, respectively. The

variation of the widths could be fitted by the log-normal distribution function:[22,23]

$$f_N = \frac{A}{w\sigma\sqrt{2\pi}} \exp\left[-\frac{\ln(w/\overline{w})^2}{2\sigma^2}\right] \tag{1}$$

where w is the width of the nanoparticles and rods, $\overline{w}$ is the mean width of the nanoparticles ($\equiv 40.7 \pm 0.5$ nm) and rods ($\equiv 0.67 \pm 0.02$ nm), A is the initial constant for the nanoparticles ($\equiv 5.56 \pm 0.59$) and rods, and σ is the standard deviation of the width distribution of the nanoparticles ($\equiv 0.18 \pm 0.02$) and rods ($\equiv 0.24 \pm 0.02$). The log-normal distribution of the width was asymmetrical for both CTO nanoparticles and

rods. The small standard deviation of the width distribution ($\sigma \leq 0.25$) illustrates that the CTO nanoparticles and rods were well confined to the limited width range. Furthermore, energy dispersive spectroscopy (EDS) measurements were performed on annealed CTO samples to confirm the removal of the EG precursor at a temperature of 600 °C. The EDS spectra in Fig. 4(c) confirms the presence of the elements Co, Ti, and O, only, which further confirms the high purity of the CTO samples.

Nitrogen adsorption–desorption isotherm measurements for the sol–gel synthesized CTO microrod shown in Fig. 5 were performed to evaluate the pore structure. The distinctive hysteresis loop was mainly observed at higher pressures, i.e., 0.0–1.0 P/P_0, indicating a type IV isotherm for the CTO microrod (Fig. 5(a)) and revealing a mesoporous structure. The pore volume and specific surface area of the CTO microrods measured from the N_2 adsorption–desorption isotherm using the Brunauer–Emmett–Teller (BET) method were 0.142 cm^3 g^{-1} and 126.89 m^2 g^{-1}, respectively. The higher surface area of the CTO microrods was attributed to the mesoporous hexagonal structure obtained after the linkage of the distinct CTO

nanoparticles. Furthermore, the pore size distribution was analyzed as a function of the pore diameter for the CTO shown in Fig. 5(b) from the desorption curve using the Barrett–Joyner–Halenda (BJH) method. The broad peak of the pore size distribution curve confirmed the presence of a wide range of pores throughout the hexagonal CTO rods. A specific surface area and total pore volume of 126.89 m^2 g^{-1} and 0.142 cm^3 g^{-1}, respectively, were observed for the hexagonal rods composed of CTO nanoparticles. The pore size distribution was confined to the range of 4 to 285 nm, with an average (mean) pore diameter distribution of 3.919 nm. Even though the largest pore diameter distribution of 285.3 nm was observed, most of the pores were in the range of 4–100 nm. The maximum number of pores had a diameter of 30.6 nm. The mesoporous CTO rods offered a larger surface area, and provided plenty of accessible sites deep inside the rod morphology for the collection of ions. Hence, it was expected to increase the interaction at the electrode–electrolyte interface. Moreover, the interconnection of the nanoparticles provided easy transportation for the ions to penetrate deep inside the mesoporous structure, and further assisted the significant improvement in the faradaic charge storage mechanism.

X-ray photoelectron spectroscopy (XPS) studies were carried out for the quantitative analysis of the electronic structure and chemical properties of the mesoporous CTO microrod. Fig. 6 shows the high-resolution XPS spectra of the core-levels of Co(2p), Ti(2p), and O(1s). The dual-peak feature of Co(2p) is shown in Fig. 6(a). The peaks corresponding to Co(2p$_{3/2}$) and Co(2p$_{1/2}$) were located at binding energies of 780.5 and 796.4 eV, respectively. The shake-up satellite peaks were observed at 786.4 and 802.6 eV, which are 5.9 and 6.2 eV higher in binding energy than that of the Co(2p$_{3/2}$) and Co(2p$_{1/2}$) peaks, respectively. The double peak feature of Co(2p) that was observed, along with the associated shake-up satellite peaks, reveals the paramagnetic chemical state of Co^{2+} and the open $3d^9$ shell of Co^{2+}, and is usually observed in divalent magnetic elements like Cu and Ni.[24] Furthermore, to precisely determine the double peak feature of Co(2p) and its shake-up satellite peak, the Co(2p) XPS spectra were decomposed via the Voigt curve fitting function, followed by a Shirley background. The Co(2p$_{3/2}$) and Co(2p$_{1/2}$) peaks were deconvoluted into four distinct peaks labeled as A, A′, C, and C′, and are located at binding energies of 780.5, 782.6, 796.4, and 798.4 eV. These four peaks (A, A′, C, and C′) represent the Co^{2+}(2p$_{3/2}$), Co^{3+}(2p$_{3/2}$), Co^{2+}(2p$_{1/2}$), and Co^{3+}(2p$_{1/2}$) peaks, respectively. The peak intensity of Co^{2+}(2p$_{3/2}$) was significantly (i.e., >2 times) larger than that of Co^{3+}(2p$_{3/2}$), indicating the presence of a substantially larger amount of Co^{2+} in the CTO. Moreover, the shake-up satellite peaks of Co(2p$_{3/2}$) and Co(2p$_{1/2}$) also decomposed into four discrete peaks identified as B, B′, D, and D′, and are located at the binding energies of 786.4, 789.8, 802.6, and 806.0 eV. B, B′, D, and D′ represent the shake-up satellite peaks of Co^{2+}(2p$_{3/2}$), Co^{3+}(2p$_{3/2}$), Co^{2+}(2p$_{1/2}$), and Co^{3+}(2p$_{1/2}$), respectively. The spin–orbit splittings between the Co(2p$_{3/2}$) and Co(2p$_{1/2}$) core levels and their shakeup satellite peaks were 15.9, and 16.2 eV, respectively, and is attributed to the presence of the larger amount of Co^{2+} than that of Co^0 or Co^{3+} ions.[15,25,26] Fig. 6(b) shows the XPS spectra of the Ti(2p) core
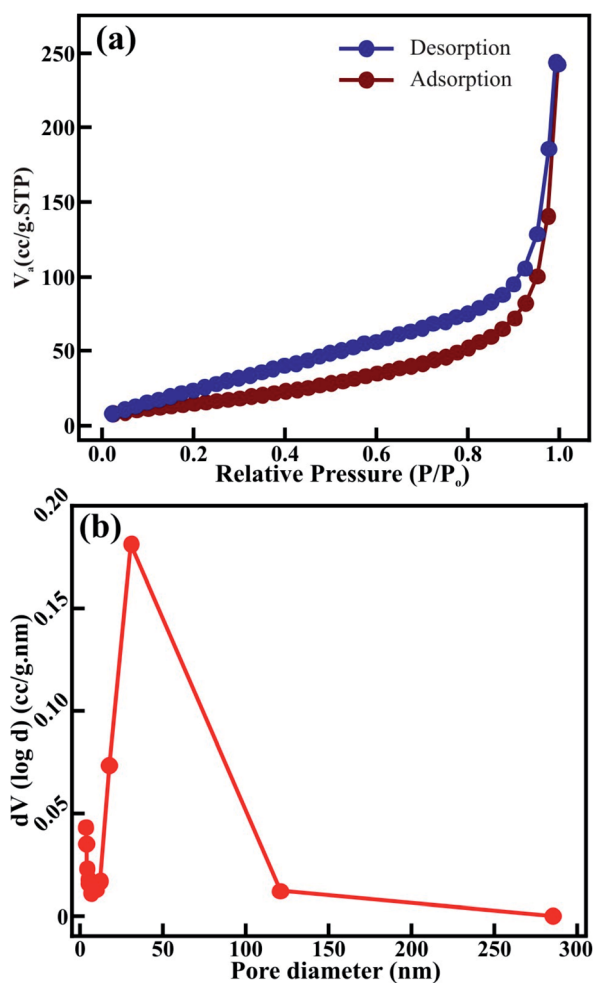

Fig. 5 (a) N_2 adsorption–desorption isotherm, and (b) BJH pore size distribution of the mesoporous CTO microrod.
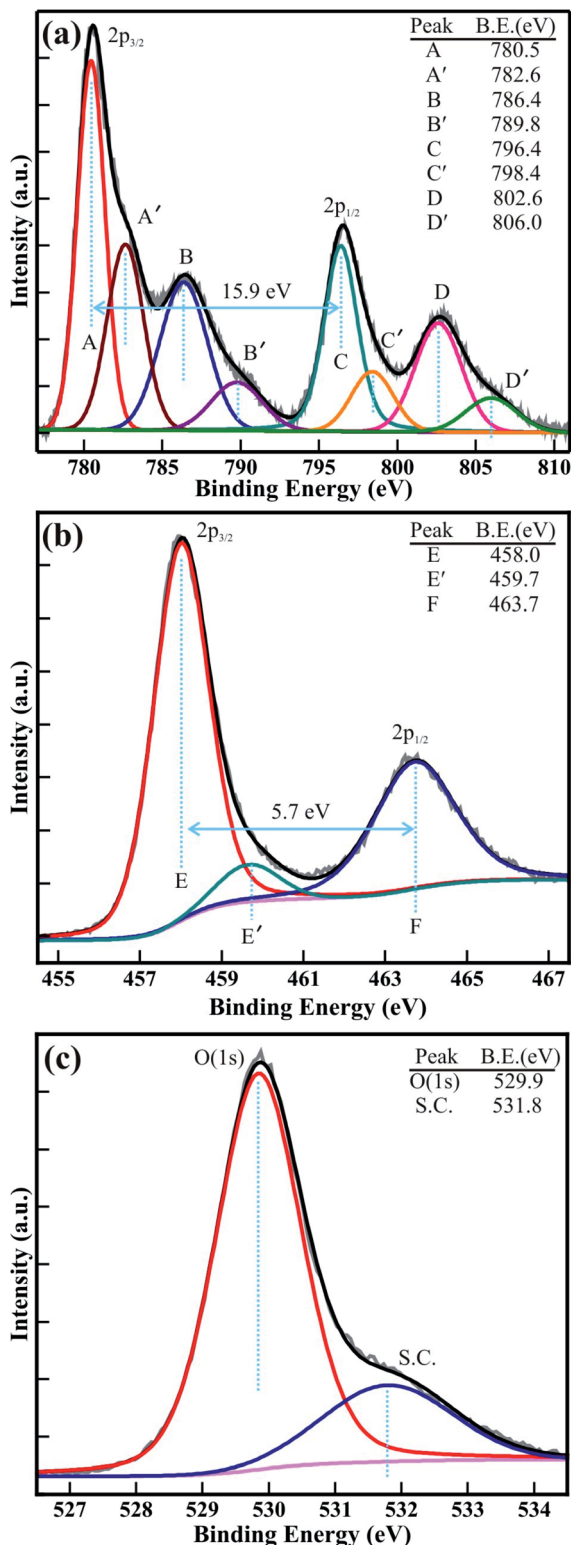
Fig. 6 Typical high-resolution XPS spectra of the (a) Co(2p), (b) Ti(2p), and (c) O(1s) core levels of the mesoporous CTO microrods.

levels, which were deconvoluted *via* Voigt curve fitting function within the Shirley background to precisely determine the double peak features of the Ti($2p_{3/2}$) and Ti($2p_{1/2}$) core levels. The decomposed peaks were observed at binding energies of

458.0 eV (*i.e.*, E), 459.8 eV (*i.e.*, E'), and 463.7 eV (*i.e.*, F), and are assigned to the Ti^{4+}($2p_{3/2}$), Ti^{3+}($2p_{3/2}$) and Ti^{4+}($2p_{1/2}$) core levels, respectively.[3,5,27] The intensity of the Ti^{4+}($2p_{3/2}$) was 12 times larger than that of Ti^{3+}($2p_{3/2}$), confirming the presence of the larger amount of Ti^{4+} and only miniscule traces of Ti^{3+}. This confirms that a very small quantity of Co^{3+} and Ti^{3+} is present in the CTO compound to achieve the stoichiometry. Furthermore, the O(1s) XPS spectra of the CTO microrod was decomposed *via* Voigt curve fitting function within the Shirley background (Fig. 6(c)), and show the perfect fits to two peaks located at 529.84 and 531.74 eV. This represents the O(1s) core level of the O^{2-} anions and the surface contamination, such as carbon oxides or hydroxides[5] in the mesoporous CTO rods. Moreover, the BE separation (ΔE) of 71.8 eV between O(1s) and Ti($2p_{3/2}$) was very close to the enthalpy of formation of CoTiO$_3$.[3] Overall, the XPS analysis confirms the formation of stable mesoporous CTO microrods consisting of a significantly larger amount of Co^{2+} and Ti^{4+} cations, and minor traces of Co^{3+} and Ti^{3+} cations.

The diffusion of a large number of ions during the charging process is expected to gain the maximum value of C_s. Therefore, wettability studies were carried out to investigate the electrode–electrolyte interface mechanism. The average contact angle determined by the Young's relation for various concentrations of aqueous KOH electrolyte (0.5 M, 1 M, 1.5 M, and 2 M) on the electrode surface confirmed their inversely proportional relation. The contact angles of the CTO microrods measured for the 0.5 M (Fig. 7(a)), 1 M (Fig. 7(b)), 1.5 M (Fig. 7(c)), and 2 M (Fig. 7(d)) concentrations of aqueous KOH electrolyte were 65.4°, 56.8°, 43.9°, and 36°, respectively. The increase in the concentration of KOH electrolyte might have led to the improved cohesive force with the CTO microrods, and were expected to further enhance the diffusion of the electrolyte/ions deep inside the mesoporous CTO microrods. Therefore, the 2 M aq. KOH electrolyte exhibiting a lower contact angle with the CTO electrode was preferred for the electrochemical measurements.

The electrochemical performance of the mesoporous CTO microrods was analyzed from cyclic voltammetry (CV), galvanostatic charge–discharge (GCD), and electrochemical impedance spectroscopy (EIS) in 2 M aq. KOH electrolyte. The CV was
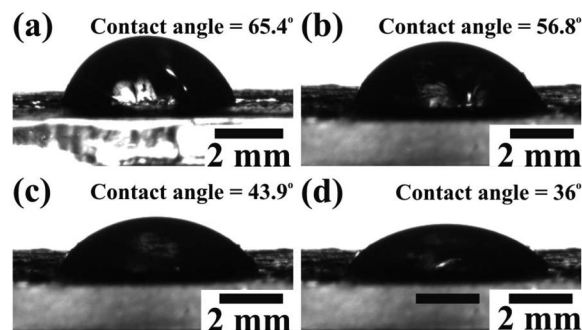

Fig. 7 Contact angle measurement showing the interface of the aqueous KOH electrolyte of (a) 0.5 M, (b) 1 M, (c) 1.5 M, and (d) 2 M concentration on the surface of the working electrode of mesoporous CTO microrods.

performed in the potential range of 0 to 0.6 V at different sweep rates, varying from 5, 10, 20, 40, 50, and 100 mV s^{-1} (Fig. 8(a)). The two distinct peaks observed at positive and negative current densities in the potential window of 0 to 0.6 V revealed the oxidation and reduction of the CTO rods, respectively. Furthermore, these oxidation and reduction peaks were shifted
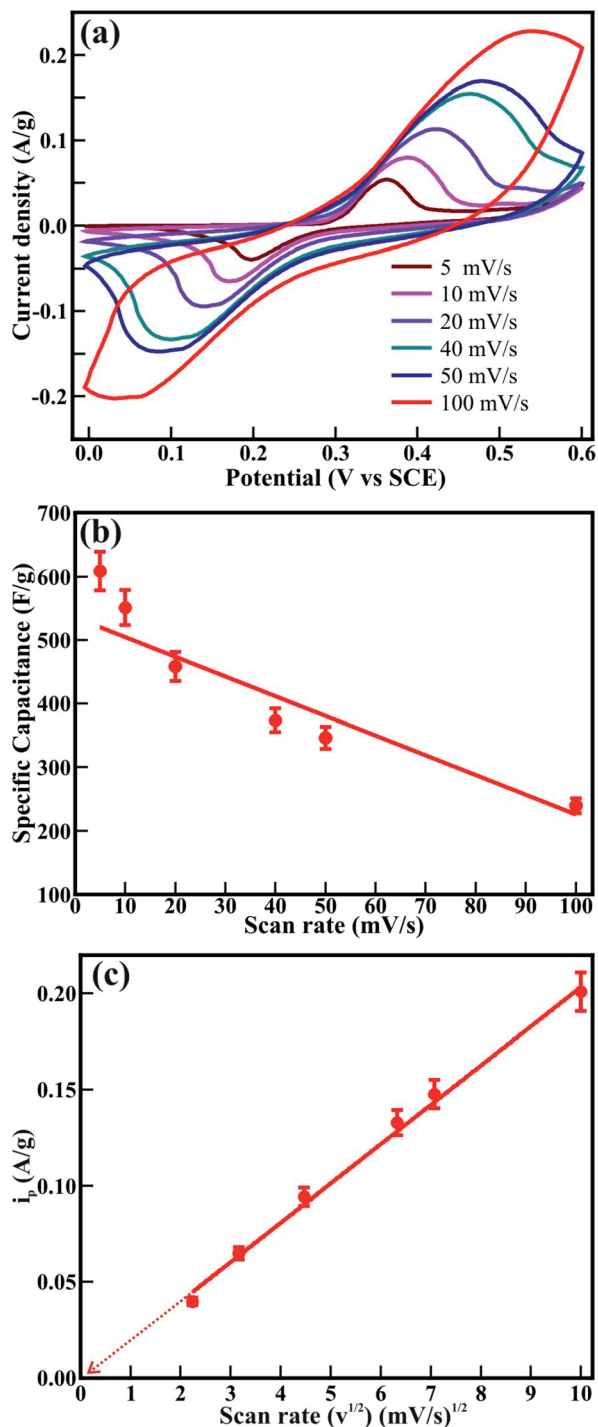

Fig. 8 (a) Cyclic voltammograms and (b) specific capacitance of mesoporous CTO microrod observed at various scan rates in 2 M aq. KOH electrolyte. (c) The graphical illustration of the anodic peak current density (i_p) with the square root of the scan rate ($v^{1/2}$).

to relatively higher and lower potentials with an increase in the sweep rate. The oxidation peak observed for the potential of 0.36 V at a sweep rate of 5 mV s^{-1} shifted by 0.17 V (*i.e.*, observed at 0.54 V) at the sweep rate of 100 mV s^{-1}. Similarly, the reduction peak observed at 0.20 V for a sweep rate of 5 mV s^{-1} was shifted by 0.17 V (*i.e.*, observed at 0.03 V) after increasing the sweep rate of 100 mV s^{-1}. This shifting in the oxidation and reduction peaks with an increase in the sweep rate was assigned to the redox processes, owing to the polarization and ohmic resistance at the electrolyte–electrode interface during faradaic processes. This is akin to the observations for the Co$_3$O$_4$ hexagonal platelets composed of nanoparticle,[28] Co$_3$O$_4$ nano-rods,[7] LaNiO$_3$ nanotubes,[29] and core–shell morphology of NiCo$_2$O$_4$ nanosheets and hollow microrod arrays.[30] Moreover, the peak intensity and area under the CV graph have increased with an increase in the sweep rate, which is indicative of the more significant diffusion of OH$^-$ ions at the slower scan rates.

The specific capacitance (C_s) shown in Fig. 8(b) was evaluated from the CV graphs at various sweep rates (Fig. 8(a)) using the equation:

$$C_S = \frac{\int i \, dV}{2mv\Delta V} \quad (2)$$

where C_s is the specific capacitance (F g^{-1}), m is the mass of the CTO microrods loaded in the working electrode (g), v is the scanning rate (mV s^{-1}), ΔV is the applied potential range (V), and $\int i \, dV$ is the integral area under the CV graph. The evaluated C_s values linearly varied with the sweep rate. The C_s value of 608.4 F g^{-1} obtained at a sweep rate of 5 mV s^{-1} was retained to 239.4 F g^{-1} even after increasing the sweep rate to 100 mV s^{-1}. The easy access of the electrolyte deep inside the mesoporous CTO microrods might have provided a preeminent diffusion of the large number of OH$^-$ ions at a slower sweep rate along the textural boundaries of the nanoparticles assembled in the mesoporous microrods, and further resulted in the larger C_s value of 608.4 F g^{-1}. The increased sweep rate was expected to restrict the easy access of larger amounts of OH$^-$ ions in a short time, and hence reduce the C_s. The C_s value of 608.4 F g^{-1} conceived from the mesoporous CTO rods was relatively larger than those of the pristine Co$_3$O$_4$ and TiO$_2$ nanostructure morphologies, such as hexagonal platelet Co$_3$O$_4$ particles (*i.e.*, 476 F g^{-1}),[28] Co$_3$O$_4$ nanorods (*i.e.*, 351 F g^{-1}),[31] mesoporous Co$_3$O$_4$ nanosheets (*i.e.*, 92 F g^{-1}),[32] brookite TiO$_2$ nanoneedles (*i.e.*, 34.1 mF g^{-1}),[5] selectively dealloyed Ti/TiO$_2$ network nanostructures (*i.e.*, 35.5 F g^{-1}),[33] and NiO@Co$_3$O$_4$ core–shell nanofibers (*i.e.*, 437 F g^{-1}).[10] Moreover, the present mesoporous CTO microrods delivered significantly larger Cs values than the hetero-architectures of Co or Ti oxides formed with other compatible metal oxides or pristine/doped graphene oxides. A hierarchical 3D flower of Co$_3$O$_4$@MnO$_2$ grown on nitrogen-doped graphene oxide (NGO) hybrid composites delivered C_s values of 347 F g^{-1}. Gobal *et al.*[34] synthesized NiO–ZnO/TiO$_2$ nanotubes, which were formed after calcination of the electro-deposited Zn–Ni over the TiO$_2$ nanotubes. These nanotubes provided Cs values of 325 F g^{-1} in a 1 M NaOH electrolyte. The agglomeration of microwave-irradiated NTO nanoparticles restricted the easy access of the 0.5 M H$_2$SO$_4$ electrolyte, and

hence constrained the redox process, further limiting the Cs value to 257 F g^{-1}.[17] Likewise, CTO provided a substantially higher Cs value than the other ABO$_3$ family members, such as LaFeO$_3$ (*i.e.*, 375.7 F g^{-1}),[35] LaNiO$_3$ (*i.e.*, 280 F g^{-1}),[29] and SrMnO$_3$ (*i.e.*, 321.7 F g^{-1}).[36] Furthermore, the variation of the current density with respect to the sweep rate was estimated by the Randle–Sevcik equation (Fig. 8(c)):

$$i_p = 2.69 \times 10^5 C_o n^{3/2} \nu^{1/2} D^{1/2} \qquad (3)$$

where i_p is the peak current density in mA g^{-1}, C_o is the concentration of OH$^-$ ions in the electrolyte solution, n is the number of electrons, ν is the sweep rate in mV s^{-1}, and D is the diffusion coefficient of the OH$^-$ ions in the electrode material. The plot of the peak current density with respect to the sweep rate shows the linear behavior. The straight line passing through the origin confirms the diffusion-controlled adsorption and desorption of OH$^-$ ions along the surface of the CTO nanoparticles assembling to form mesoporous microrods.

Fig. 9(a) shows the charge–discharge curves measured at various current densities, ranging from 30 to 120 mA g^{-1}. The asymmetric behavior of the charge–discharge plots revealed the pseudocapacitive behavior of the mesoporous CTO microrods. Fig. 9(b) shows the specific capacitance (F g^{-1}) at different current densities estimated from the equation:

$$C_s = \frac{I dt}{m dv} \qquad (4)$$

The maximum C_s of 299.5 F g^{-1} gained for the current density of 30 mA g^{-1} was reduced to 230.4 F g^{-1} at the current density to 120 mA g^{-1} (Fig. 9(b)). The time provided for the diffusion of ions deep inside the mesoporous microrods along the surface of the CTO nanoparticles was relatively small at the higher current density. That is why the C_s values were reduced with an increase in the current density. The C_s value of 299.5 F g^{-1} achieved from the mesoporous CTO microrods was significantly higher than the values reported for the other perovskites of di- and tri-valent metal ions, such as the PVP-assisted porous LaCoO$_3$ nanospheres (*i.e.*, 203 F g^{-1} in 6 M KOH),[37] electro-deposited LaMnO$_3$/MnO nanoarrays on carbon cloth (*i.e.*, 260 F g^{-1} in 0.5 M Na$_2$SO$_4$),[38] hydrothermally derived nanotube of Co@TiO$_2$ and RGO composite (*i.e.*, 27.5 F g^{-1}),[9] and sol–gel assisted Sr-doped LaMnO$_3$ spheres (*i.e.*, 198 F g^{-1}).[39] Moreover, the mesoporous CTO rods provided better Cs values than the nanocomposite prepared by varying the composition of the constituent phases of carbon, Fe$_2$O$_3$, and Co$_3$O$_4$. The Cs value of C/Fe$_2$O$_3$ (*i.e.*, 85.3 F g^{-1}) was further improved after the addition of Co$_3$O$_4$ (*i.e.*, 144 F g^{-1}).[40] This reaffirmed that the CTO microrods were excellent electrode materials from the perovskite family in its pristine form.

The longer cyclic stability was essential for the better durable performance of the supercapacitor. Therefore, the cycling stability of the mesoporous CTO microrods was tested at a current density of 100 mA g^{-1} for 1950 charge–discharge cycles (Fig. 9(c)). The C_s values of 299.5 F g^{-1} were reduced by ~2% for the initial 1000 cycles, which was further lowered by
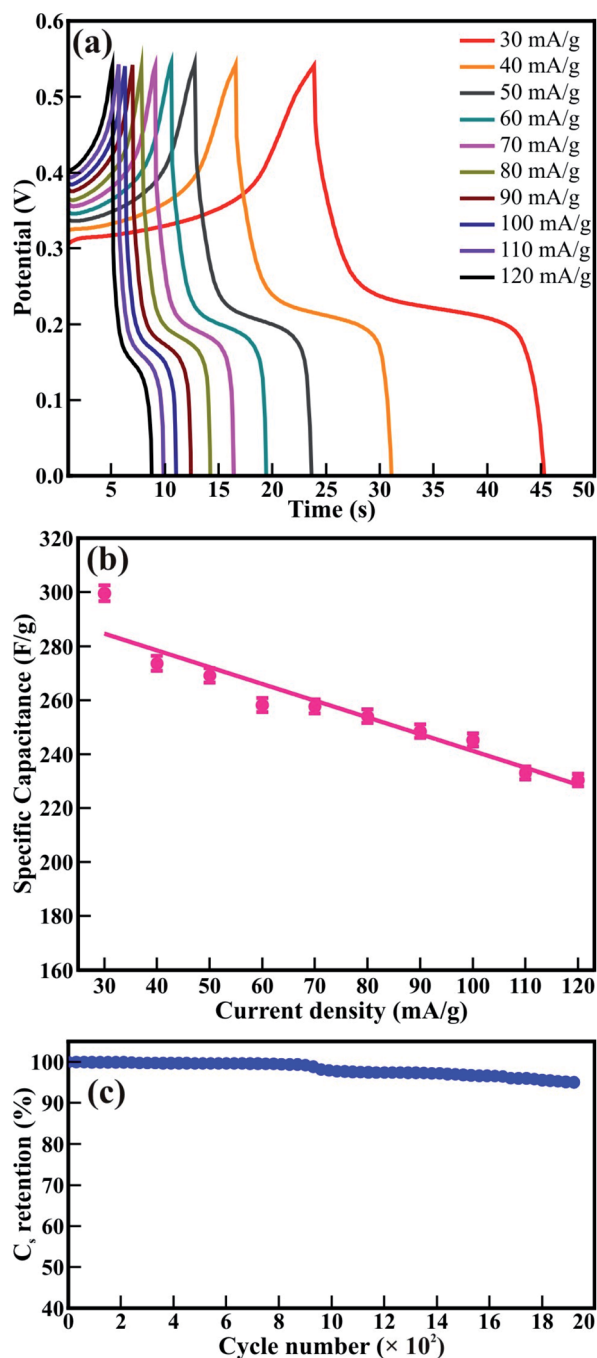

Fig. 9 (a) GCD curves and (b) evaluated specific capacitance of mesoporous CTO rods at various current densities. (c) Specific capacitance retention analyzed for 1950 GCD cycles at the current density of 100 mA g^{-1}. The inset figure shows the first 10 cycles.

~5% after the 1950 continuous charge–discharge cycles. The observed capacitance retention for the mesoporous CTO microrods was more impressive than the values attained for the microwave-irradiated NTO nanoparticles[17] and the electro-deposited LaMnO$_3$/MnO nanoarrays.[38] It was also compatible with the hierarchical flower-like 3D nanostructure of the Co$_3$O$_4$@MnO$_2$/nitrogen-doped graphene oxide hybrid composite[41] and the mesoporous perovskite of interlocked NiTiO$_3$

nanoparticles.[42] This distinct cyclic stability of the mesoporous CTO microrods confirms the better durability, longer lifetime, and excellent electrochemical stability in the 2 M KOH electrolyte.

The surface morphology, textural boundaries, and electrical properties of the active electrode material play a vital role in the diffusion of the ions from the electrolyte. Therefore, electrochemical impedance spectroscopy (EIS) was employed to know the contribution of textural boundaries and electrical resistance in the diffusion of OH^- ions in the mesoporous CTO microrods. Fig. 10(a) demonstrates the typical Nyquist plots of the CTO microrods in 2 M KOH electrolyte. The EIS spectrum of the mesoporous CTO microrods before the stability study is akin to that recorded after the stability study for 1950 charging–discharging cycles. The EIS spectra signify a perfect fit for the semicircular arc analogous to the charge-transfer resistance at the interface of the electrolyte and CTO microrods. This semicircular arc of the impedance spectra is similar to the Co_3O_4,[7] TiO_2,[5] $LaMnO_3/MnO$,[38] and Sr-doped $LaMnO_3$.[39] The intercept and diameter of the semicircular arc symbolizing the charge transfer resistance (R_{ct}) of 92.1 Ω for mesoporous CTO microrods has been reduced to 41.2 Ω after 1950 charge–discharge cycles. However, the values of the electrolyte resistance (R_s) obtained before the stability study (1.33 Ω) remained the same even after 1950 continuous charging–discharging cycles (1.37 Ω). The equivalent circuit for the EIS consists of the electrolyte resistance (R_s), charge transfer resistance (R_{ct}), and constant phase elements denoted in the inset of Fig. 10(a). It confirms that the larger surface area, in conjunction with the clearly visible textural boundaries of the interconnected nanoparticles of the mesoporous CTO microrods, provides abundant access to the OH^--ions from the aq. KOH electrolyte. The partial drop in the charge diffusion of the mesoporous CTO microrods after 1950 cycles indicates the increase in the accessibility of the surface and textural boundaries of the mesoporous CTO rods during repeated charge–discharging cycles, which might be one of the reasons behind the excellent stability. The time constant was calculated to divulge the reaction kinetics for the transport of the OH^- ions deep inside the CTO microrods from the equation:

$$\tau = \frac{1}{2\pi f^*} \tag{5}$$

where f^* is the frequency corresponding to the maxima of the imaginary component of the semicircle. The measured value of the time constant of 1.32 μs (before the stability study) confirmed the abrupt and easy access for the OH^--ions to transport deep inside the CTO microrod along the textural boundaries. The time constant was not reduced even after 1950 charging–discharging cycles (i.e., 1.59 μs), reinforcing the excellent cyclic stability observed for the mesoporous CTO microrods.

Fig. 10(b) exhibits the relation of the specific power and specific energy evaluated from eqn (6) and (7) to interpret the comprehensive performance of CTO,

$$E = \frac{1}{2} \times C_s \times (\Delta V)^2 \tag{6}$$

$$P = \frac{E}{\Delta t} \times 3600 \tag{7}$$

where C_s is the specific capacitance (F g^{-1}), ΔV is the potential operating range (volts), Δt is the discharge time in (s), P is the specific power (W kg^{-1}), and E is the specific energy (W h kg^{-1}). The specific power reduces with respect to an enhancement in the specific energy, as the charge/discharge current density increased from 30 to 120 mA g^{-1}. The maximum specific power of 4835.7 W kg^{-1} and a specific energy of 9.8 W h kg^{-1} was obtained from mesoporous CTO. The specific power of 4835.7 W kg^{-1} (at the current density of 30 mA g^{-1}) obtained for CTO was significantly higher than the hierarchical flower-like 3D nanostructure of the Co_3O_4@MnO_2/nitrogen-doped graphene oxide hybrid composite (i.e., 850 W kg^{-1}),[41] 3D TiO_2@-$Ni(OH)_2$ core–shell nanowire arrays (i.e., 1881.8 W kg^{-1}),[11] and 3D nanonet of hollow structured Co_3O_4 (i.e., 100 W kg^{-1}).[43] Moreover, the performance of mesoporous CTO was relatively excellent in comparison with the perovskites of $NiCo_2O_4$
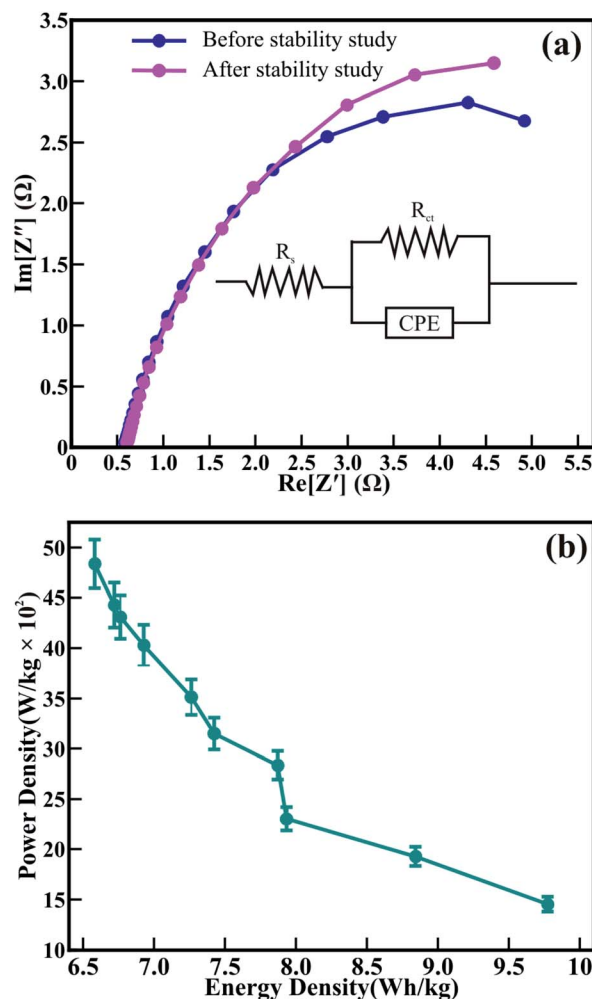

Fig. 10 (a) Nyquist (EIS) plot of the mesoporous CTO microrods obtained before and after cyclic stability studies. Inset shows the best fitted equivalent circuit model. (b) Evaluated specific energy and specific power of the mesoporous CTO microrods.

nanosheets@ hollow microrod arrays (*i.e.*, 100 W kg^{-1}),[30] Sr-doped LaMnO$_3$ nanoparticles (*i.e.*, 120 W kg^{-1}),[39] and 3D carbon-fiber network anchored with metallic Co (*i.e.*, 797 W kg^{-1}),[44] and was compatible with the mesoporous perovskite of interlocked NiTiO$_3$ nanoparticles (4320 W kg^{-1}).[42] The improved electrochemical performance of CTO is attributed to the well-connected network of CTO nanoparticles, well defined textural boundaries, and highly accessible larger surface area of the perforated mesoporous morphology, collectively furnishing the easy access for ion diffusion deep inside the mesoporous structure.

4   Conclusions

In conclusion, we report the synthesis of mesoporous cobalt titanite (CTO) microrods incorporating interconnected nanoparticles with clearly visible textural boundaries. The CTO nanoparticles of average diameter ∼59 nm were hierarchically organized in the hexagonal form, and provided mesoporous microrods of average diameter ∼800 nm and an average pore size distribution of 3.919 nm throughout the rod body. The CTO nanoparticles of the mesoporous rods are of the hexagonal crystalline phase to the space group of $R\bar{3}$. XPS analysis showed the consistent presence of Co^{2+}/Co^{3+} and Ti^{4+}/Ti^{3+}, confirming the formation of stoichiometric CTO microrods. The interconnection of the CTO nanoparticles resulted in the formation of mesoporous CTO rods with increased textural boundaries, and offered a larger surface area for significantly larger diffusion of OH$^-$ ions. This further led to an increase in the C_s value in 2 M KOH electrolyte. The diffusion-controlled access to the OH$^-$ ions (0.27 µs) deep inside the rod structure provided a higher specific power (4835.7 W kg^{-1}) and specific energy (9.77 W h kg^{-1}) than the other perovskite family members. Moreover, the excellent stability for up to 1950 continuous charging–discharging cycles with the capacitance retention of 82.3% demonstrates that the mesoporous CTO microrods are a proficient working electrode for the supercapacitor. Furthermore, the morphology-dependent electrochemical performance shown in this study has unlocked a new corridor to explore the core–shell hetero-architectures of CTO rods with other metal oxides like TiO$_2$, MnO$_2$, and CuO as an electrode for hybrid capacitors, which may further enhance the electrochemical performance.

Conflicts of interest

There are no conflicts to declare.

Acknowledgements

References

1 K. Narasimharao, P. R. Chikate, R. A. Patil, Y. R. Ma, P. M. Shirage and R. S. Devan, *CrystEngComm*, 2019, **21**, 7130–7140.

2 C. Duan, J. Tong, M. Shang, S. Nikodemski, M. Sanders, S. Ricote, A. Almansoori and R. O' Hayre, *Science*, 2015, **349**, 1321–1326.

3 K. Narasimharao, R. S. Kalubarme, P. R. Chikate, C. J. Park, Y. R. Ma, P. M. Shirage and R. S. Devan, *ChemistrySelect*, 2019, **4**, 6620–6626.

4 R. S. Devan, R. A. Patil, J. H. Lin and Y. R. Ma, *Adv. Funct. Mater.*, 2012, **22**, 3326–3370.

5 R. S. Devan, Y. R. Ma, R. A. Patil and S. M. Lukas, *RSC Adv.*, 2016, **6**, 62218–62225.

6 X. Lu, G. Wang, T. Zhai, M. Yu, J. Gan, Y. Tong and Y. Li, *Nano Lett.*, 2012, **12**, 1690–1696.

7 T. Jiang, S. Yang, Z. Bai, P. Dai, X. Yu, M. Wu and H. Hu, *Nanotechnol*, 2018, **29**, 315402.

8 T. Arun, T. K. Kumar, R. Udayabhaskar, R. V. Mangalaraja and A. A. Fakhrabadi, *Mater. Res. Express*, 2019, **6**, 0850b1.

9 H. Xiao, W. Guo, B. Sun, M. Pei and G. Zhou, *Electrochim. Acta*, 2016, **190**, 104–117.

10 P. Jiang, Q. Wang, J. Dai, W. Li and Z. Wei, *Mater. Lett.*, 2017, **188**, 69–72.

11 Q. Ke, M. Zheng, H. Liu, C. Guan, L. Mao and J. Wang, *Sci. Rep.*, 2015, **5**, 13940.

12 M. DiDomenico Jr. and S. H. Wemple, *Phys. Rev.*, 1968, **166**, 565.

13 F. Hu, H. Zhang, C. Sun, C. Yin, B. Lv, C. Zhang, W. W. Yu, X. Wang, Y. Zhang and M. Xiao, *ACS Nano*, 2015, **9**, 12410–12416.

14 M. Mizumaki, K. Yoshii, Y. Hinatsu, Y. Doi and T. Uruga, *Phys. Scr., T*, 2005, **115**, 513–515.

15 M. Shilpy, M. A. Ehsan, T. H. Ali, S. B. A. Hamid and M. E. Ali, *RSC Adv.*, 2015, **5**, 79644–79653.

16 C. N. R. Rao, P. Ganguly, K. K. Singh and R. A. M. Ram, *J. Solid State Chem.*, 1988, **72**, 14–23.

17 M. Imani, L. Radmanesh and A. Tadjarodi, *Ceram. Int.*, 2019, **45**, 18772–18777.

18 P. Kakvand, M. S. Rahmanifar, M. F. El-Kady, A. Pendashteh, M. L. Kiani, M. Hashami, M. Najafi, A. Abbasi, M. F. Mousavi and R. B. Kaner, *Nanotechnol*, 2016, **27**, 315401.

19 Z.-D. Huang, T.-T. Zhang, H. Lu, J. Yang, L. Bai, Y. Chen, X.-S. Yang, R.-Q. Liu, X.-J. Lin, Y. Li, P. Li, X. Liu, X.-M. Feng and Y.-W. Ma, *Sci. China Mater.*, 2018, **61**, 1057–1066.

20 Y.-J. Lin, Y.-H. Chang, W.-D. Yang and B.-S. Tsai, *J. Non-Cryst. Solids*, 2006, **352**, 789–794.

21 G.-W. Zhou, D. K. Lee, Y. H. Kim, C. W. Kim and Y. S. Kang, *Bull. Korean Chem. Soc.*, 2006, **27**, 368–372.

22 P. R. Chikate, K. D. Daware, S. S. Patil, P. N. Didwal, G. S. Lole, R. J. Chaudhary, S. W. Gosavi and R. S. Devan, *New J. Chem.*, 2020, **44**, 5535–5544.

23 R. S. Devan, W. D. Ho, S. Y. Wu and Y. R. Ma, *J. Appl. Crystallogr.*, 2010, **43**, 498–503.

24 J. S. Shaikh, R. C. Pawar, R. S. Devan, Y. R. Ma, P. P. Salvi, S. S. Kolekar and P. S. Patil, *Electrochim. Acta*, 2011, **56**, 2127–2134.

25 J. Anirudha, P. T. Rao, N. Munichandraiah and S. A. Shivashankar, *J. Electroanal. Chem.*, 2016, **761**, 21–27.

26 G. Yang, W. Yan, J. Wang and H. Yang, *Mater. Lett.*, 2014, **122**, 117–120.

27 R. S. Devan, Y. R. Ma, M. A. More, R. T. Khare, V. V. Antad, R. A. Patil, V. P. Thakare, R. S. Dhayal and L. S. Mende, *RSC Adv.*, 2016, **6**, 98722–98729.

28 K. Deori, S. K. Ujjain, R. K. Sharma and S. Deka, *ACS Appl. Mater. Interfaces*, 2013, **5**, 10665–10672.

29 K. H. Ho and J. Wang, *J. Am. Ceram. Soc.*, 2017, **100**, 4629–4637.

30 X.-F. Lu, D.-J. Wu, R.-Z. Li, Q. Li, S.-H. Ye, Y.-X. Tong and G.-R. Li, *J. Mater. Chem. A*, 2014, **2**, 4706–4713.

31 F. Manteghi, S. H. Kazemi, M. Peyvandipour and A. Asghari, *RSC Adv.*, 2015, **5**, 76458–76463.

32 S. Xiong, C. Yuan, X. Zhang, B. Xi and Y. Qian, *Chem.–Eur. J.*, 2009, **15**, 5320–5326.

33 P.-C. Chen, S.-J. Hsieh, J. Jou and C.-C. Chen, *Mater. Lett.*, 2014, **133**, 175–178.

34 F. Gobal and M. Faraji, *Electrochim. Acta*, 2013, **100**, 133–139.

35 Z. Li, W. Zhang, C. Yuan and Y. Su, *RSC Adv.*, 2017, 7, 12931–12937.

36 G. George, S. L. Jackson, C. Q. Luo, D. Fang, D. Luo, D. Hu, J. Wen and Z. Luo, *Ceram. Int.*, 2018, **44**, 21982–21992.

37 Y. Guo, T. Shao, H. You, S. Li, C. Li and L. Zhang, *Int. J. Electrochem. Sci.*, 2017, **12**, 7121–7127.

38 P. Ma, N. Lei, B. Yu, Y. Liu, G. Jiang, J. Dai, S. Li and Q. Lu, *Nanomater*, 2019, **9**, 1676.

39 X. W. Wang, Q. Q. Zhu, X. E. Wang, H. C. Zhang, J. J. Zhang and L. F. Wang, *J. Alloys Compd.*, 2016, **675**, 195–200.

40 J. Su, S. Liu, J. Wang, C. Liu, Y. Li and D. Wu, *MRS Commun.*, 2016, **6**, 367–374.

41 S. Ramesh, K. Karuppasamy, H.-S. Kim, H. Kim and J.-H. Kim, *Sci. Rep.*, 2018, **8**, 1–11.

42 N. Kitchamsetti, Y. R. Ma, P. M. Shirage and R. S. Devan, *J. Alloys Compd.*, 2020, **833**, 155134.

43 Y. Wang, Y. Lei, J. Li, L. Gu, H. Yuan and D. Xiao, *ACS Appl. Mater. Interfaces*, 2014, **6**, 6739–6747.

44 A. P. Tiwari, S. H. Chae, G. P. Ojha, B. Dahal, T. Mukhiya, M. Lee, K. Chhetri, T. Kim and H. Y. Kim, *J. Colloid Interface Sci.*, 2019, **553**, 622–630.